The Astrophysical Journal Letters, 856:L17 (10pp), 2018 March 20 https://doi.org/10.3847/2041-8213/aab436
© 2018. The American Astronomical Society.
OPEN ACCESS

Determination of Differential Emission Measure from Solar Extreme Ultraviolet Images

Yang Su[1,2], Astrid M. Veronig[3], Iain G. Hannah[4], Mark C. M. Cheung[5], Brian R. Dennis[6], Gordon D. Holman[6], Weiqun Gan[1,2], and Youping Li[1,2]
[1] Key Laboratory of Dark Matter and Space Astronomy, Purple Mountain Observatory, Chinese Academy of Sciences (CAS), 8 Yuanhua Road, Nanjing 210034, People's Republic of China; yang.su@pmo.ac.cn
[2] School of Astronomy and Space Science, University of Science and Technology of China, Hefei, Anhui 230026, People's Republic of China
[3] Kanzelhöhe Observatory-IGAM, Institute of Physics, University of Graz Universitaetsplatz 5/II, Graz A-8010, Austria
[4] SUPA School of Physics & Astronomy, University of Glasgow, Glasgow G12 8QQ, UK
[5] Lockheed Martin Solar & Astrophysics Laboratory, 3251 Hanover Street, Palo Alto, CA 94304, USA
[6] Solar Physics Laboratory (Code 671), Heliophysics Science Division, NASA Goddard Space Flight Center, Greenbelt, MD 20771, USA
Received 2018 January 23; revised 2018 March 4; accepted 2018 March 5; published 2018 March 23

Abstract

The Atmospheric Imaging Assembly (AIA) on board the *Solar Dynamic Observatory* (*SDO*) has been providing high-cadence, high-resolution, full-disk UV-visible/extreme ultraviolet (EUV) images since 2010, with the best time coverage among all the solar missions. A number of codes have been developed to extract plasma differential emission measures (DEMs) from AIA images. Although widely used, they cannot effectively constrain the DEM at flaring temperatures with AIA data alone. This often results in much higher X-ray fluxes than observed. One way to solve the problem is by adding more constraint from other data sets (such as soft X-ray images and fluxes). However, the spatial information of plasma DEMs are lost in many cases. In this Letter, we present a different approach to constrain the DEMs. We tested the sparse inversion code and show that the default settings reproduce X-ray fluxes that could be too high. Based on the tests with both simulated and observed AIA data, we provided recommended settings of basis functions and tolerances. The new DEM solutions derived from AIA images alone are much more consistent with (thermal) X-ray observations, and provide valuable information by mapping the thermal plasma from ∼0.3 to ∼30 MK. Such improvement is a key step in understanding the nature of individual X-ray sources, and particularly important for studies of flare initiation.

Key words: magnetic reconnection – methods: data analysis – Sun: corona – Sun: flares – Sun: UV radiation – Sun: X-rays, gamma rays

1. Introduction

The differential emission measure (DEM) diagnostic (Golub et al. 2004; Weber et al. 2004) from a set of extreme ultraviolet (EUV) or soft X-ray (SXR) images taken at different spectroscopic lines or narrowband filters has been a useful tool for studying flare plasma and energetics. The DEM describes the amount of thermal plasma along the line of sight (LOS) as a function of T. Given a DEM(T) (in unit of $cm^{-5}\,K^{-1}$), other parameters can be estimated, such as plasma density, thermal X-ray flux, thermal energy, and emission measure (EM)-weighted temperatures, etc. Therefore, it could provide strong aid to X-ray studies, where heated plasma is one of the major sources of flare X-ray emissions.

The thermal and non-thermal X-rays originate from different populations of electrons. In practice, these components in X-ray spectra are usually determined from spectral fitting to the spatially integrated (count) spectrum. However, the fitting results are model-dependent. In addition, the spatially integrated spectra provide limited information on individual sources in X-ray images, which are directly related to energy release and particle acceleration/transportation in reconnections.

The best way to study the nature of flare X-ray sources is through the analysis of imaging spectroscopy. Only the *Ramaty High Energy Solar Spectroscopic Imager* (*RHESSI*; Lin et al. 2002) currently provides such data, but it has only been able to study a small number of events in high detail due to its limited sensitivity, dynamic range, and time coverage. Direct focusing X-ray telescopes such as the proposed *Focusing Optics X-ray Solar Imager* (*FOXSI*) mission (Christe et al. 2016) could alleviate these problems. In this paper we present a DEM approach with current EUV/SXR data to help improve the understanding of flare X-ray emission. We should however point out that x-ray data is still required to study both the non-thermal and thermal emission in flares.

The DEM solutions derived from current methods (see the benchmark test, Aschwanden et al. 2015) using solely Atmospheric Imaging Assembly (AIA; Lemen et al. 2012) filtergrams are not always well constrained. They often show more plasma at flaring temperatures (from ∼6 MK to tens of MK) than is expected. These artificial high-temperature components contribute little to AIA intensities due to AIA's relatively weak responses in this temperature range, but would result in much higher X-ray emissions than observed, as X-ray fluxes are very sensitive to these temperatures.

In Figure 1 we show an example of such a situation. The AIA data was taken on 2013 November 13 09:01:30 UT (Figure 2(a)), minutes before the start of a *Geostationary Operational Environmental Satellite* (*GOES*) C-class flare. To be consistent with the low level of X-ray emission, there should be very little plasma above 10 MK. But the DEM solutions derived from three popular DEM codes (using AIA data only and the default settings), the regularized inversion code (Hannah & Kontar 2012), the XRT_dem_iterative2 (Weber et al. 2004), and the sparse inversion code (Cheung et al. 2015), show significant amount of plasma above 10 MK (Figure 1(a)). As a result, the X-ray spectra emitted from these plasma are at

Original content from this work may be used under the terms of the Creative Commons Attribution 3.0 licence. Any further distribution of this work must maintain attribution to the author(s) and the title of the work, journal citation and DOI.

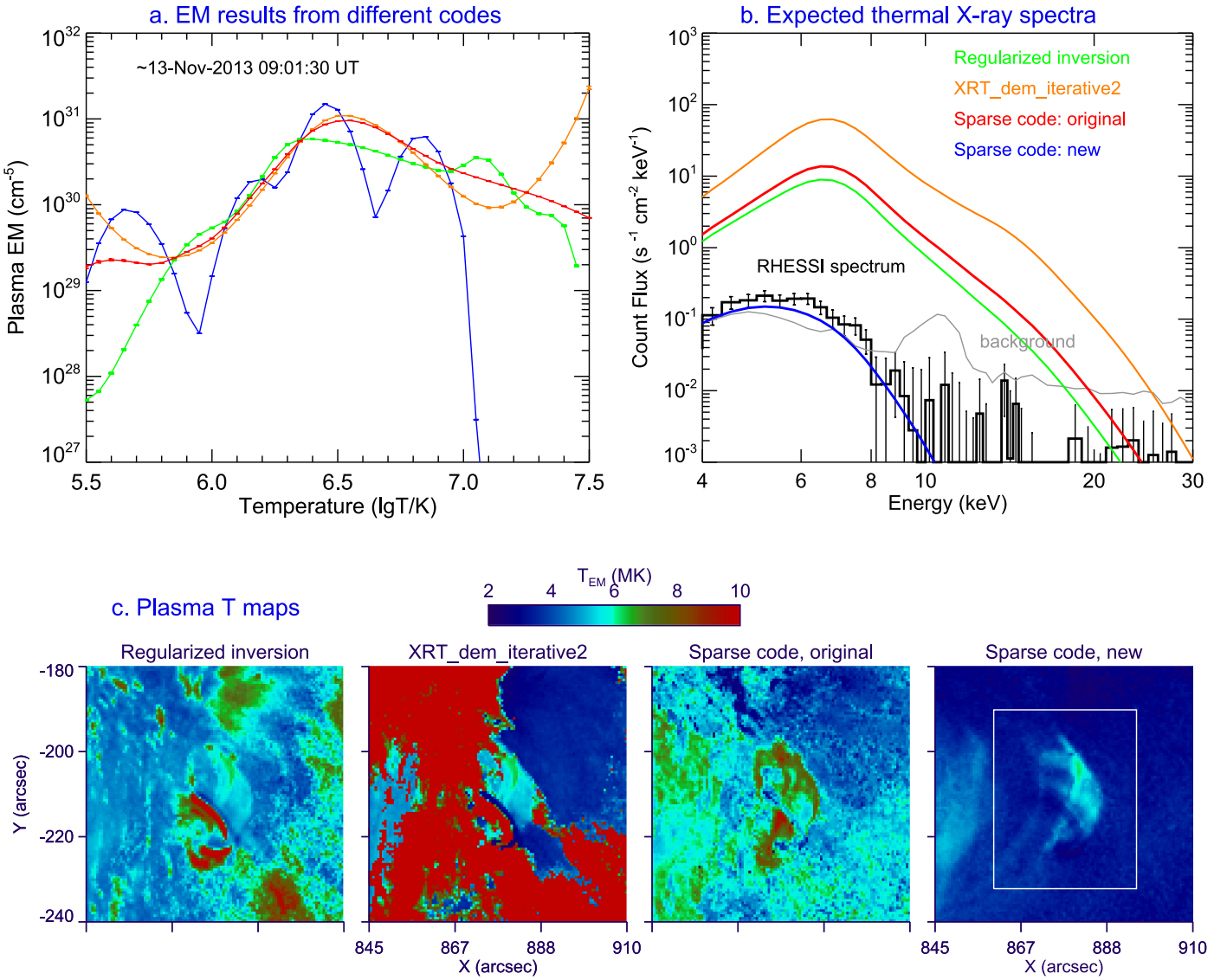

Figure 1. Comparison of DEM results from four methods. The methods include: the regularized inversion code, the XRT_dem_iterative2, the original sparse inversion code, and the sparse inversion code with new settings. The AIA images used here were taken at ~2013 November 13 09:01:30 UT (Figure 2(a)). (a) Comparison of plasma EM distribution over T. The curves are integrated in the region marked by the white rectangle in Figures 1(c). (b) Thermal X-ray spectra calculated from the EM results as would be observed by *RHESSI*. The observed, background-subtracted count spectrum (histogram in black) is made from *RHESSI* detector 6. (c) EM-weighted temperature (T_{EM}) maps. All of the negative DEMs in the solutions of the regularization inversion code are set to 0. The errors on DEM/EM are calculated from a Monte Carlo method, which runs the new code for 100 times by adding random noises to the observed intensities.

least an order of magnitude higher than the full-disk spectrum observed by *RHESSI* (Figure 1(b)). The EM-weighted temperature T_{EM} maps show very different distributions of flare plasma (Figure 1(c)). These results could lead us to erroneous in studies of plasma heating, especially pre-flare heating. Adding more constraint from other datasets (such as soft X-ray images and fluxes, Battaglia & Kontar 2013; Warren et al. 2013; Caspi et al. 2014; Inglis & Christe 2014; Motorina & Kontar 2015) may solve the problem. But the spatial information of plasma DEM are lost in many cases.

In this work, we aim to derive more accurate DEM from AIA images alone, so that we could take advantages of the good time coverage of AIA data for statistical studies. The data sets and instruments we used are described in Section 2. In Section 3, we discuss on the problems of current DEM methods and present the new settings for the sparse inversion code. It was tested with both simulated and observed data. The results from different methods are compared in Section 4. Furthermore, we applied the code to two flares (Section 5). Conclusions, discussion, and limitations of the code are given in Section 6 and the Appendix.

2. Instruments and Data Processing

RHESSI was launched in 2002 and is still operational. It obtains spectra and indirect images of the flaring Sun with high-energy resolution (as high as ~1 keV) and spatial resolution (as high as 2.″3) in both X-rays and gamma-rays, from ~3 keV to 17 MeV.

In this Letter, *RHESSI* light curves are obtained from the "full_rate" quick-look data, which provides light curves from user-defined detectors. *RHESSI* images were reconstructed using the Clean algorithm available in the Solar SoftWare

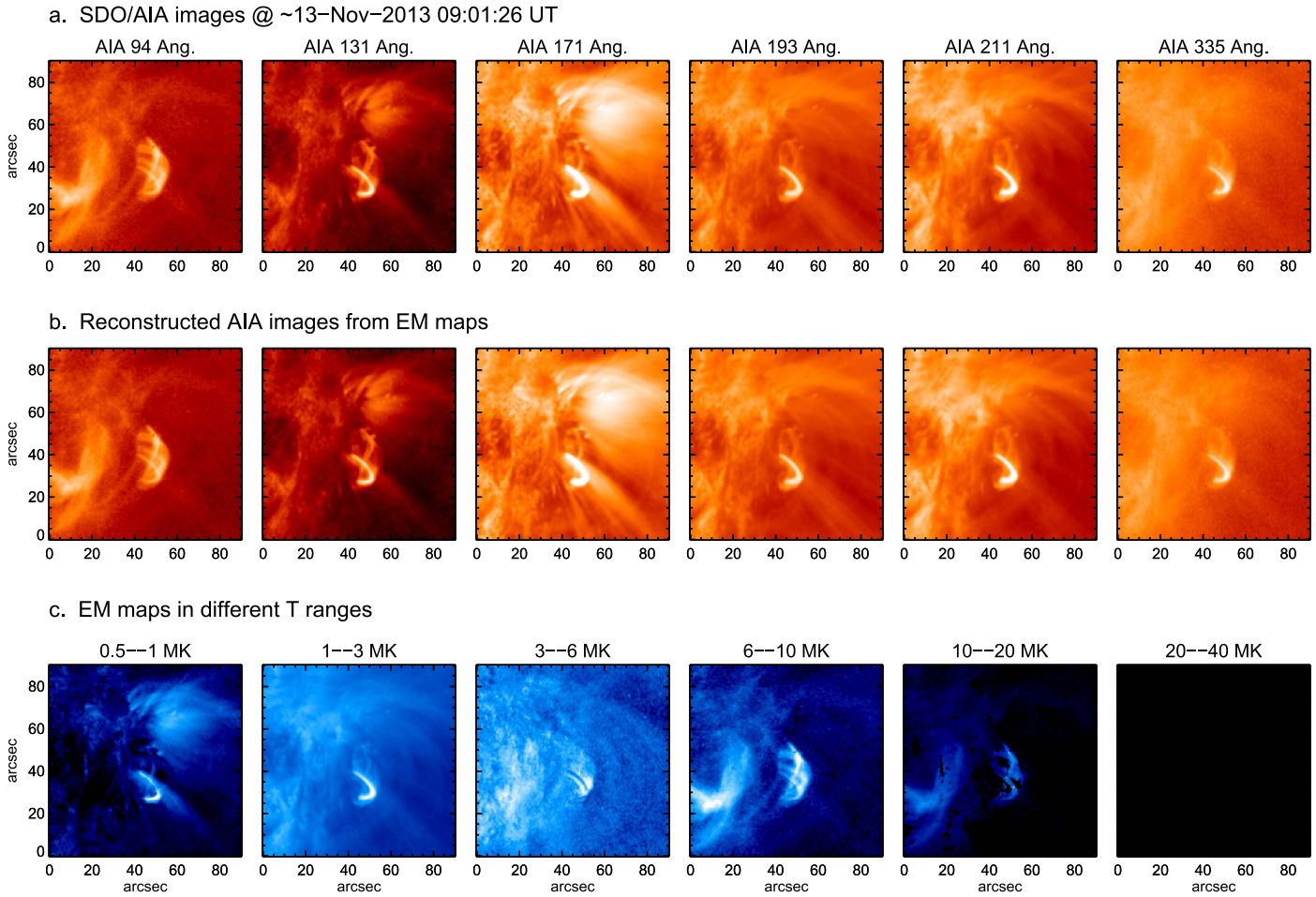

Figure 2. Example of AIA images, reconstructed AIA images, and EM maps at different temperatures. The DEM solution is derived from the sparse inversion code with the new settings. (a) AIA observations in six channels taken at ∼2013 November 13 09:01:30 UT. (b) Reconstructed AIA images from DEM solutions. (c) Plasma EM_T maps at different temperature ranges. The new results show that the bright loop-like structure is actually a cool loop at coronal temperatures.

(SSW). *RHESSI* spectra were made from a single detector and analyzed in the OSPEX package.

The *Solar Dynamic Observatory* (*SDO*; Pesnell et al. 2012)/AIA has been imaging the full solar disk in ten UV-visible/EUV channels since 2010, with high spatial (∼1.2 arcsec) and temporal (∼12 s in EUV channels) resolutions. AIA images are processed to level 1.5 and aligned onto a common platescale using "AIA_prep.pro" in SSW. The errors on the AIA intensities in both simulated data and observed data are estimated from the function "aia_bp_estimate_error" provided by the *SDO* package in the SSW, which takes a number of instrumental effects into account.

According to the document "GOES_XRS_readme.pdf" at the *GOES* website (https://ngdc.noaa.gov/stp/satellite/goes/index.html), the archived fluxes for *GOES* 8–15 have had SWPC (NOAA Space Weather Prediction Center) scaling factors applied. In order to get the true fluxes, we divided the *GOES* data in 1–8 Å by a factor of 0.7. This factor has been recently confirmed by the well calibrated SXR spectral measurements taken from the *Miniature X-ray Solar Spectrometer (MinXSS-1) CubeSat* mission (above C1 level, see details in Woods et al. 2017).

The XRT (Golub et al. 2007) on the *Hinode* (Solar-B; Kosugi et al. 2007) takes SXR images of the solar corona. The data is processed by the "xrt_prep" and "xrt_deconvolve." A known problem with XRT is that its temperature response (TR) functions are systematically lower than those expected in the DEM studies using other data sets, such as AIA EUV images and *Hinode*/EIS data (Testa et al. 2011; Cheung et al. 2015; Schmelz et al. 2015). In this work, we followed Wright et al. (2017) and multiplied the XRT TR by a factor of 2 when creating the expected XRT image from DEM results.

3. The New Settings for the Sparse Inversion Code

Emission measure within a certain temperature range $EM_T = DEM(T) \cdot \Delta T = \int n_e^2 dl$ describes the amount of plasma integrated along the LOS over the unit area, where ΔT is the temperature bin size (K), n_e is the electron number density. For a single pixel, DEM(T) are calculated from a set of intensities (I, in DN/s) taken in the six AIA channels (94, 131, 171, 193, 211, and 335 Å). Given the TR of each channel, one can derive the DEMs by solving a set of equations: $\sum DEM(T) \cdot \Delta T \cdot TR = I$.

The main reason why the current methods fail to constrain the DEMs is the relatively weak response of AIA at high temperatures. But there are also reasons related to the methods. The regularized inversion will provide a mathematically correct solution with $\chi^2 = 1$ for the AIA data but may include non-existent high-temperature emission or non-physical negative values. The latter can be minimized by invoking an iterative

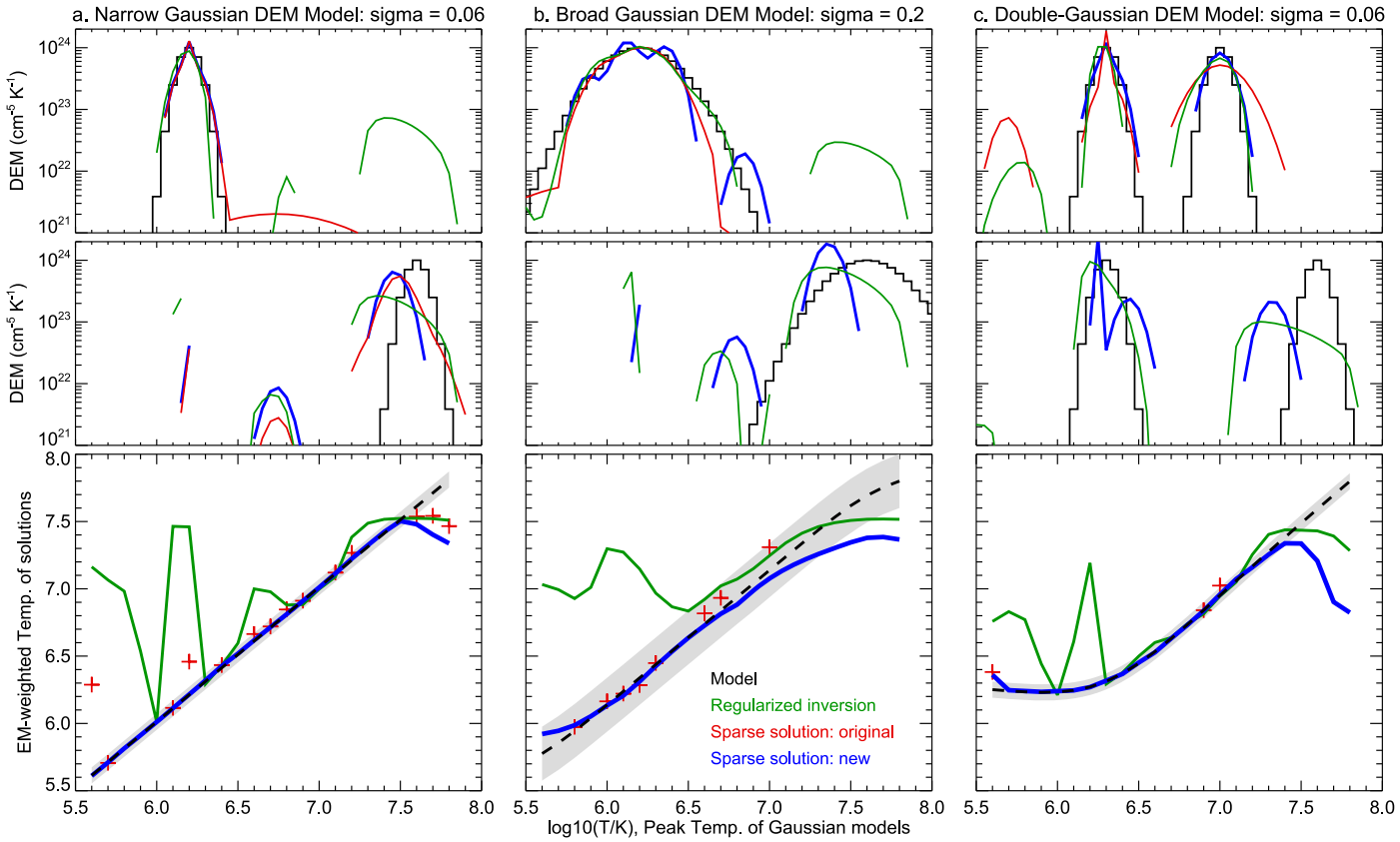

Figure 3. Tests of three DEM codes with Gaussian DEM models. The models include: a single Gaussian model with (a) $\sigma = 0.06$, (b) $\sigma = 0.2$, and (c) double-Gaussian DEM model with $\sigma = 0.06$. The peak temperatures vary from $\log_{10} T = 5.6$ to 7.6 (in model c, one Gaussian peaks at a fixed $\log_{10} T = 6.3$). Top row: DEM solutions for Gaussian models (black) peak at $\log_{10} T = 6.2$ (7.0 in panel c). The solutions from the regularized inversion are shown in green, the original sparse inversion code in red crosses (the code did not find solutions for all the tests), and the sparse inversion code with new settings in blue. Middle row is the same as top row, but for Gaussian models peak at $\log_{10} T = 7.6$. Bottom row: comparison of the $T_{\rm EM}$ derived from the solutions and the models. The dashed lines show the expected relation between peak temperatures and $T_{\rm EM}$. The area in gray shows the range of expected values $\pm\sigma$.

approach, increasing the χ^2 value until a positive DEM is achieved, but will still produce high-temperature components unless additional constraints are in place. Similarly, the XRT_dem_iterative2 approach, which involves spline fitting, will produce broad and smooth DEMs from the AIA data alone, resulting in large high-temperature components.

The sparse inversion code (version 0.91, written in IDL) is an inversion method developed for the DEM determination from a few data points, which is an underdetermined linear system. It is based on the concept of sparsity and uses the "simplex" function in the IDL data analysis package to derive a solution from AIA (and XRT) images by minimizing the sum of EM_T. The solution (if found) satisfies the observations within a certain range between max(0, I − tol) and I + tol, where tol is the tolerance on the reconstructed intensities. The code provides fast calculations of EMs and naturally ensures positive solutions. It has been tested against models and observations of non-flaring active regions (see more details in Cheung et al. 2015).

The default setting of the basis function is Dirac-delta functions plus a set of Gaussians with $\sigma = 0.1$, 0.2 and 0.6. It covers situations from narrow (isothermal plasma) to broad DEM distributions (multi-thermal plasma). Users can choose the sets of Gaussians with different widths or even other types of basis functions, but the coefficients and the number of functions used to form a linear combination for the solution are chosen by the L1-norm minimization (the simplex algorithm in this case). We suspect that the use of broad Gaussians (in some cases) may have prevented rapid drop-off toward high temperatures in the DEM distribution and caused the artificial component at high temperatures.

Therefore, we changed the basis function in the new settings to use only Dirac-delta functions and narrow Gaussians with $\sigma = 0.1$. Whether or not this is a better model to describe the plasma in the solar corona needs to be tested. We also changed the tolerances and set upper limits on them, to make sure that the differences between the reconstructed intensities and the observed values are relatively small. All of the major changes we made to the code are listed below.

1. The basis functions are set to Dirac-delta functions plus Gaussians with a sigma of 0.1, meaning that only the narrow (isothermal and nearly isothermal) components are considered. The new setting allows fast drop-off of DEM distribution at high temperatures when necessary.
2. The tolerance in the original setting is determined by tol = tolfac · σ_I, where tolfac is a user-defined constant (1.4 by default) and σ_I the uncertainty of the measured intensities I. It could be much larger than the observed I for pixels that have low counts (see Figure 4). In the new settings, tolfac is dependent on the intensities I. If no

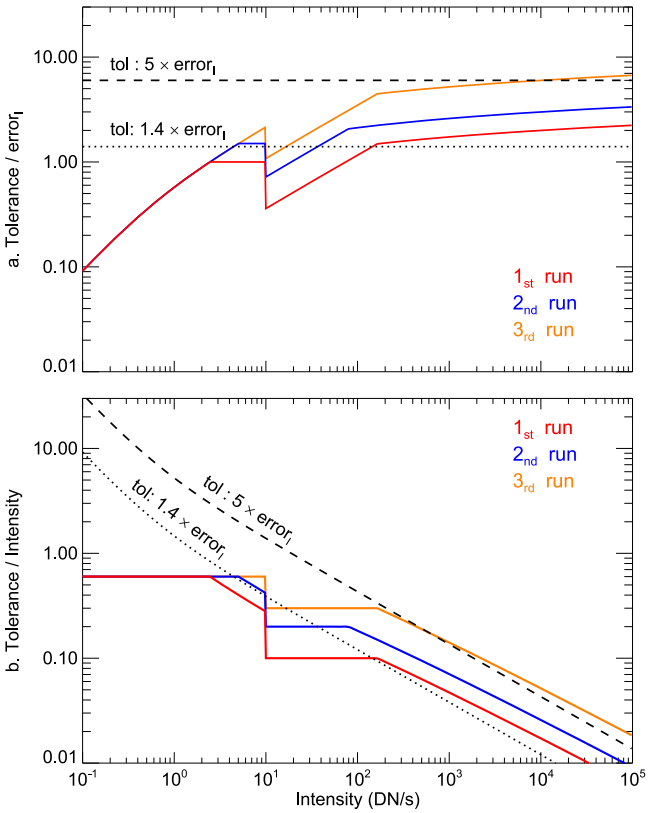

Figure 4. Example of the tolerances in the original and new settings for the sparse inversion method. Here the channel is assumed to be the AIA 131 Å and duration is one second. (a) The tolerances as a function of intensities I (tol = tolfac × σ_I, where σ_I is the uncertainty on I, and tolfac is a user-defined factor). The dotted and dashed curves show the tolerances with tolfac of 1.4 and 5 in the original setting, respectively. The new tolfac varies with I, and are increased for the two additional runs (blue and orange lines), in case no solution is found in the first run (red lines). (b) Same as the plot in (a) but for the tolerances in units of intensities I. It shows that the tolerance could be much larger than I itself in the original setting when the intensity is low, but is limited within a certain fraction of I in the new setting.

solution is found in the first run, the code will run for two additional times with increased tolerances. This allows the code to find solution in more situations.

3. Upper limits on the tolerances are set for each run of the code, to ensure that the deviations of the reconstructed intensities are within certain fractions of the input I. If a channel has total counts (DN) that are smaller than 10, then its upper limit stays at 60%, regardless of the number of runs. Otherwise, the upper limit increases from 10% to 20%, and 30% for the second and third runs (Figure 4), respectively.
4. The temperature bin size in $\log_{10} T$ is changed from 0.1 to 0.05, same as in the AIA temperature response functions. This ensures that the full TR functions are used in the calculation.

These changes allow the code to find solutions for more pixels and keep relatively small deviations of the reconstructed intensities from the input. This is important for constraining plasma DEM at high T when a pixel has low intensities in the channels sensitive to hot plasma, such as AIA 94 and 131 Å. The IDL code with the new settings will be available at http://solar.pmo.ac.cn/ysu/dem/, and can be additionally downloaded at http://aia.lmsal.com/public/results.htm.

4. Test Results

We tested the new settings with both simulated AIA data and observed AIA data. The new results are compared with those from other methods.

4.1. Tests with Gaussian DEM Models

We first tested the code for three cases, which simulate three different DEM distributions with simple Gaussian models. Case (1) includes a narrow Gaussian component with $\sigma = 0.06$ to simulate nearly isothermal plasma. Case (2) includes a broad Gaussian component with $\sigma = 0.2$, to simulate multi-thermal plasma. In the two cases, the peak temperature of the Gaussian component is adjusted from $\log_{10} T$ 5.6 to 7.7, with a step of 0.1. Case (3) includes two narrow Gaussians with $\sigma = 0.06$. One peaks at a fixed temperature $\log_{10} T = 6.3$, a simulation of plasma in the quiet corona. The other one peaks at a varying temperature from $\log_{10} T = 5.6$ to 7.7.

In each test, simulated AIA data were created from the model and the AIA TR, and then used as input for three DEM methods, the regularized inversion code, the sparse inversion code with the original settings, and the sparse code with the new settings. The DEM solutions are calculated in the $\log_{10} T$ range from 5.5 to 7.9 and then compared with the models. Examples of the comparison for the cases where the varying component peaks at $\log_{10} T = 6.2$ and 7.6 are shown in the top and middle panels of Figures 3(a)–(c). We also computed and compared the EM-weighted temperatures $T_{\rm EM}$ (Equation (1)) from the solutions and the models (Figure 3, bottom row).

$$T_{\rm EM} = \frac{\sum ({\rm DEM}(T) \cdot \Delta T \cdot T)}{\sum ({\rm DEM}(T) \cdot \Delta T)} = \frac{\sum ({\rm EM}_T \cdot T)}{\sum {\rm EM}_T} \qquad (1)$$

The results suggest that the improved sparse inversion code is, overall, better than other methods. It finds solutions for all of the tests, and produced consistent $T_{\rm EM}$ with those expected from the narrow input models in $\log_{10} T = 5.6$ to ~7.5. For broad DEM models (Figure 3(b)), the consistency is good in a shorter T range, where it tries to reproduce the broad models with multiple narrow Gaussians. Above $\log_{10} T$ 7.5, none of the methods are enable to derive good solutions. In the Appendix, we list a number of possible reasons. The most important reason is that the AIA filters have low sensitivity above $\log_{10} T = 7.5$.

4.2. Test with Flare Data

We tested the new settings with the AIA EUV images taken on 2013 November 13 ~09:01:30 UT, the same data used in Figure 1. The input AIA images, reconstructed images, and resulted EM$_T$ maps are shown in Figure 2. The DEM calculation was done for the range of $\log_{10} T$ from 5.5 to 7.5. Compared with other results, the new solution (Figure 1(a)) shows greatly reduced EM at flaring temperatures.

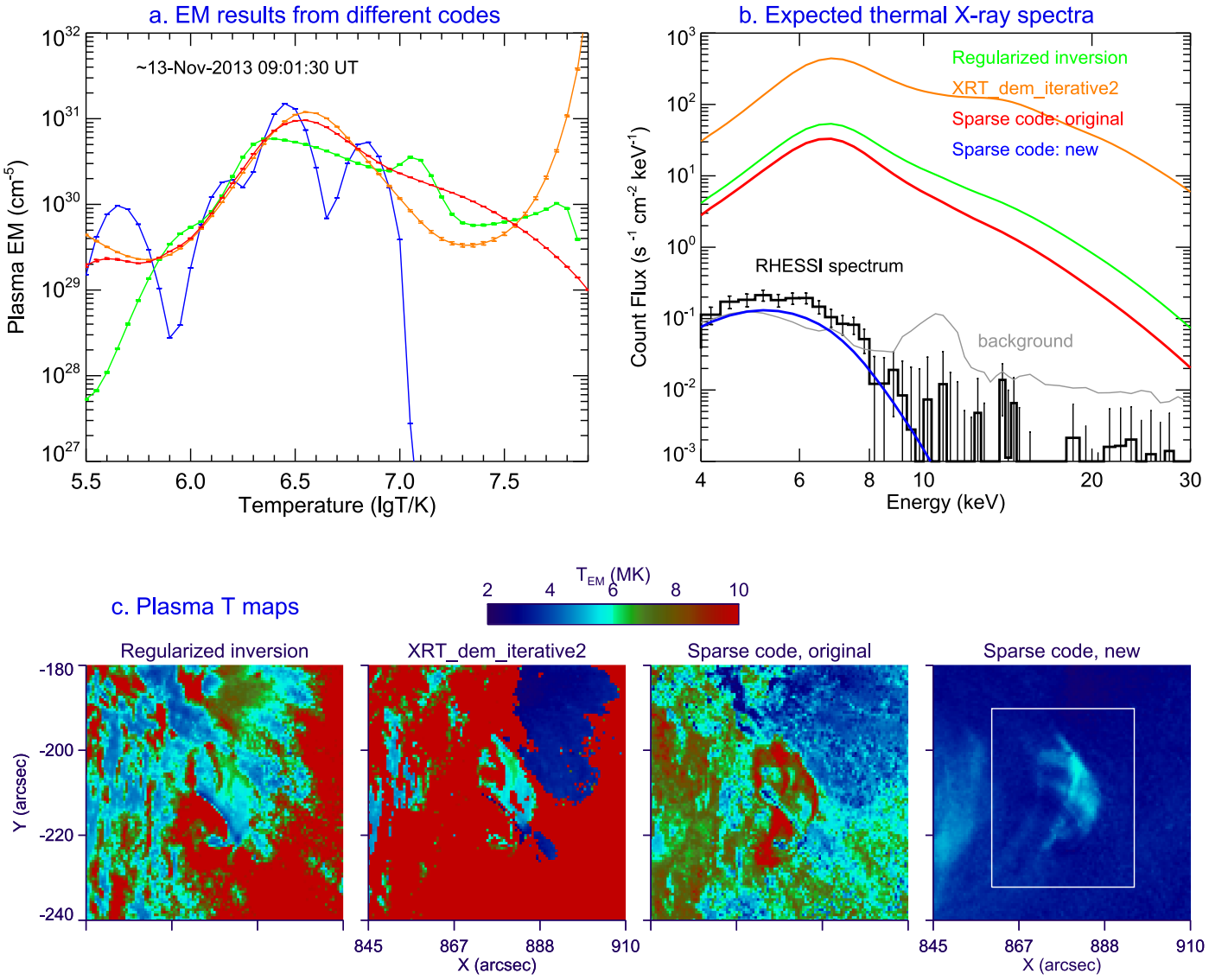

Figure 5. Same as Figure 1 but for DEM solutions derived in the $\log_{10} T$ range of 5.5–7.9.

In order to compare the results with observations, we calculated the thermal X-ray bremsstrahlung radiation spectrum for each pixel to get the spectra maps $f_{\rm th}(x, y, E)$, where x and y are the solar coordinates, and E is the X-ray photon energy in keV. The total spectrum is then obtained from the region marked in Figure 1(c). It is clear that the new spectrum (in blue, Figure 1(b)) is much more consistent with *RHESSI* data.

The original and new results differ not only in the amount of hot plasma, but also in the spatial distributions (Figure 1(c)). The $T_{\rm EM}$ maps from the original methods show that the plasma temperatures exceed 6 MK and even 10 MK in a large fraction of the region, but the new map shows no structures above 6 MK. These results would lead to distinct conclusions, especially in the studies of plasma heating in magnetic reconnection and initiation of flares.

We also tested all of the methods in the $\log_{10} T$ range from 5.5 to 7.9, and provided another figure (Figure 5) similar to Figure 1. The DEM solutions from the original methods result in even higher X-ray fluxes, but the new DEM solution does not change much.

5. Comparison with X-Ray Data

In order to further test the new settings with EUV and X-ray data, we selected two small flares (to minimize problems brought by saturated AIA pixels).

(1) Flare SOL2013-12-10T06:54 (*GOES* class C2.0) occurred at S10W62. It was reported as a well-observed reconnection event (Zhu et al. 2016). *RHESSI* did not observe useful X-ray data in this flare due to the use of an attenuator.

We first computed the EM maps from the AIA images and derived $T_{\rm EM}$ maps. The $T_{\rm EM}$ map in the rising phase (Figure 6(b)) shows heated plasma in the current sheet and both cusps. We also calculated the expected thermal X-ray flux in 1–8 Å. Its time evolution matches well with the observed *GOES* X-ray light curve (background subtracted).

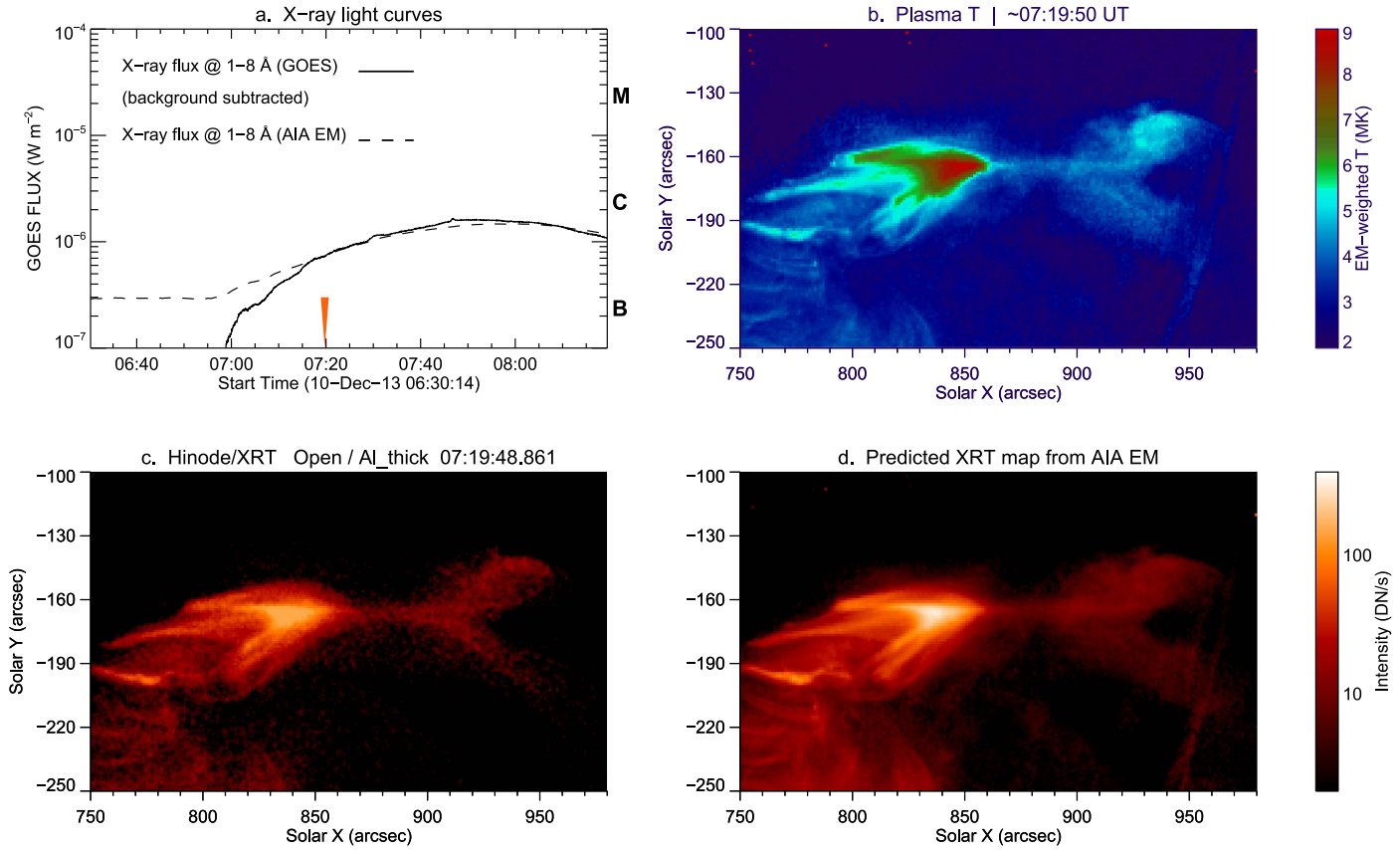

Figure 6. Comparison of EM results with X-ray data for the 2013 December 10 flare. (a). X-ray light curves in 1–8 Å calculated from AIA EM maps and observed by *GOES*. A background selected at ∼06:30 UT is subtracted from the *GOES* fluxes. (b). An example of $T_{\rm EM}$ maps in the rising phase (marked in panel a). (c). Deconvolved "Al_thick" image observed at ∼07:19:49 UT by *Hinode*/XRT. (d). Predicted "Al_thick" image from AIA EM maps. The XRT temperature response function used here was multiplied by a factor of 2, as suggested by Wright et al. (2017).

We further derived the expected XRT "Al_thick" image from the EM maps at ∼07:19:50 UT (Figure 6(d)). It is almost identical to the image observed by the *Hinode*/XRT (Figure 6(c)). The significant difference between the two images is seen in the southwest corner, along the solar limb. The limb shows up in the calculated image as a faint curve, indicating the existence of small amount of plasma at ∼4 MK. But no such trace is found in the observed XRT image, at least not at this level of intensity. This might be caused by the long integration distance (along the LOS) through the low solar atmosphere right above the solar limb, where the EUV emission may not be optically thin.

The comparisons show that the new DEM solutions are consistent with X-ray data, and that thermal emission dominate the X-rays in this flare.

(2) The other flare SOL2013-11-13T09:08 (C2.4), occurred at S11W67, shows clear enhancement of hard X-rays (HXR) at energies up to ∼50 keV. It is used to test the DEM solutions in the presence of non-thermal X-rays. Here we focus only on the pre-flare phase and the first HXR peak at ∼09:08:54 UT, because saturation of AIA pixels became a problem thereafter.

The 3–12 keV light curves calculated from the AIA DEMs are close to those observed by *RHESSI* (Figure 7(a)). At higher energies, the calculated values are much less than the observed values. This is expected because the background and non-thermal emission, which are not considered in the AIA DEMs, dominate in this energy range, *GOES* fluxes are much higher than the calculated ones, mainly due to the fact that *GOES* fluxes contain sources in other regions.

The observed *RHESSI* spectrum at the first peak are plotted in Figure 7(b). The green curve shows the calculated thermal X-ray spectrum from AIA EM maps. Their difference, shown in purple, is expected to be the non-thermal component. The spectral fitting to it with a thick-target model indicates a low energy cutoff of ∼18.4 keV and electron distribution index 4.0.

The 4–10 keV map calculated from the AIA DEM maps shows a similar loop structure to the *RHESSI* observations, but the two footpoints are not observed (Figures 7(c)–(d)). They are also the places where saturated AIA pixels are found in 171 and 193 Å channels (Figure 8(c)), which may have introduced the inaccurate DEM. Therefore, in the footpoints the thermal X-ray emission calculated from the AIA DEMs may be overestimated. At higher energies, most sources seen in the observations are absent in the calculated maps, suggesting a significant level of non-thermal emission in these sources.

(3) Another way to study plasma heating is to learn from the time history. In Figure 8 we plot the time evolution of EM_T for different locations in the two flares. These plots directly show the heating and cooling processes of flare plasma.

In the first flare (Figure 8(b)), both temperatures in the cusp and current sheet increased, but exceeded 10 MK at different time. The plasma outside the flare region was not heated during

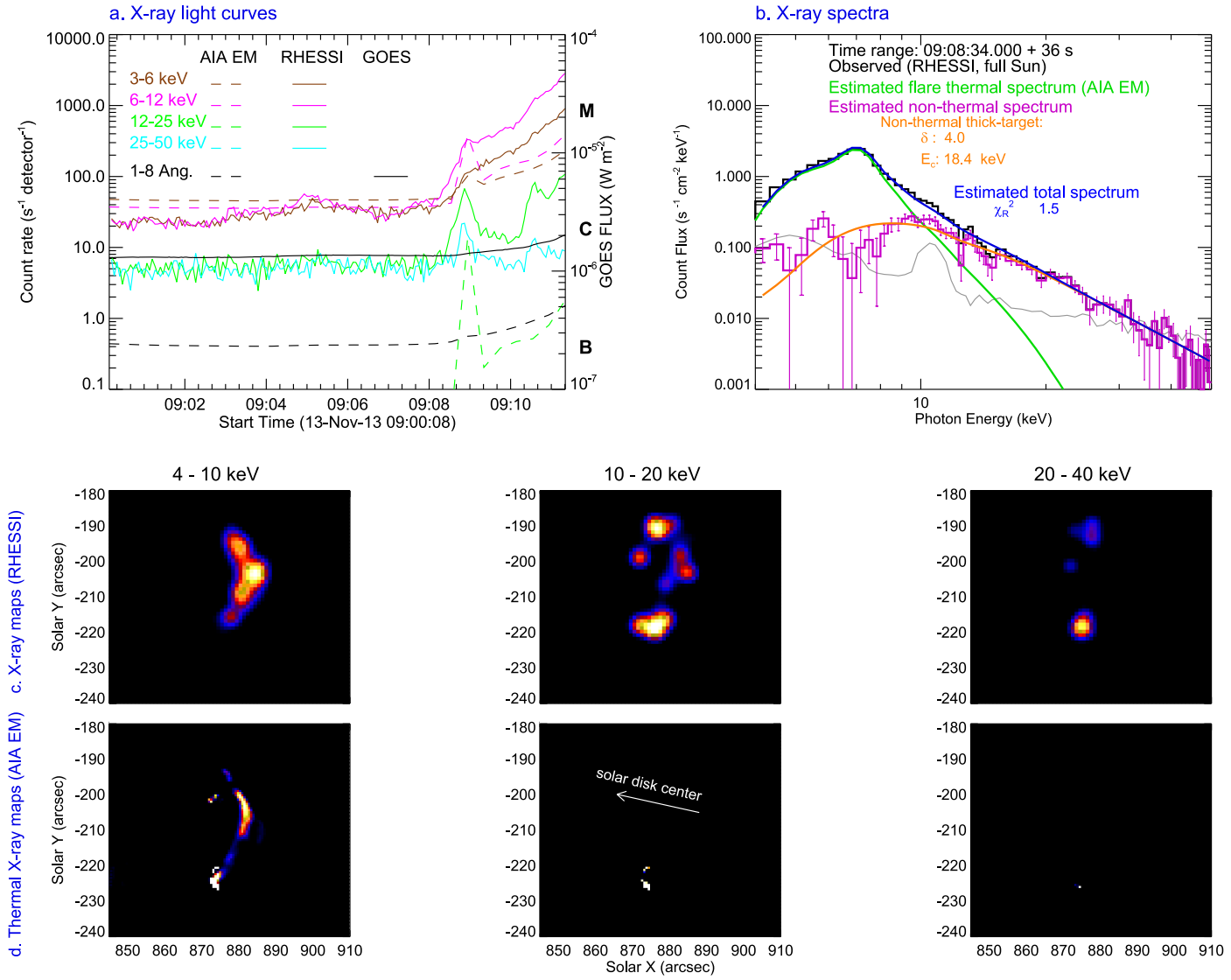

Figure 7. Comparison of EM results with X-ray data for the 2013 November 13 flare. (a). Calculated thermal X-ray light curves and observed data by *RHESSI* and *GOES*. (b). Observed *RHESSI* spectrum (black) and calculated thermal X-ray spectrum from DEM solutions (green). (c). *RHESSI* images and calculated images in different energy ranges. *RHESSI* Clean images were made for the time range between 09:08:34 and 09:09:10 UT with detectors 1 through 9, excluding 2.

the flare and remained nearly isothermal at the quiet-corona temperature ∼2.5 MK. This is different from the result in Figure 5(b) of Zhu et al. (2016) that shows a significant DEM component around 10 MK, which we believe is introduced by the method they used.

In the southern footpoint of the 2013 November 13 flare, where non-thermal emission is found to be the strongest (Figure 7(c)), plasma temperature rises rapidly to a value of ∼28 MK. It does support fast heating from the injection of non-thermal electrons, which is expected from the standard picture of flares (Shibata & Magara 2011). However, the temperature in this case approaches the super-hot temperature of 30 MK (Lin et al. 1981; Caspi & Lin 2010) that is usually seen in coronal sources of some large flares. Other observations of impulsive heating at footpoints show temperatures only around 10 MK (McTiernan et al. 1993; Hudson et al. 1994; Khan et al. 2004; Milligan & Dennis 2009). As mentioned above, the saturation of AIA pixels may play a role here. More case studies are needed to confirm this finding.

6. Summary and Discussion

We have modified the sparse inversion code to use new basis functions and tolerance control. The code was tested with both simulated and observed AIA data. Based on the results, we summarize our findings below.

(1) The DEM solutions derived by the sparse inversion code with the new settings from AIA images alone are much more consistent with thermal X-ray observations. It suggests that coronal plasma within a small confined area (such as a pixel) can be well represented by a number of narrow, nearly isothermal components. (2) The new setting works best for DEM that contains only narrow components. It is therefore ideal for obtaining DEMs from individual pixels, but not from spatially integrated intensities over a large region, as the DEM(T) distribution is more likely to be broad. (3) The time evolutions

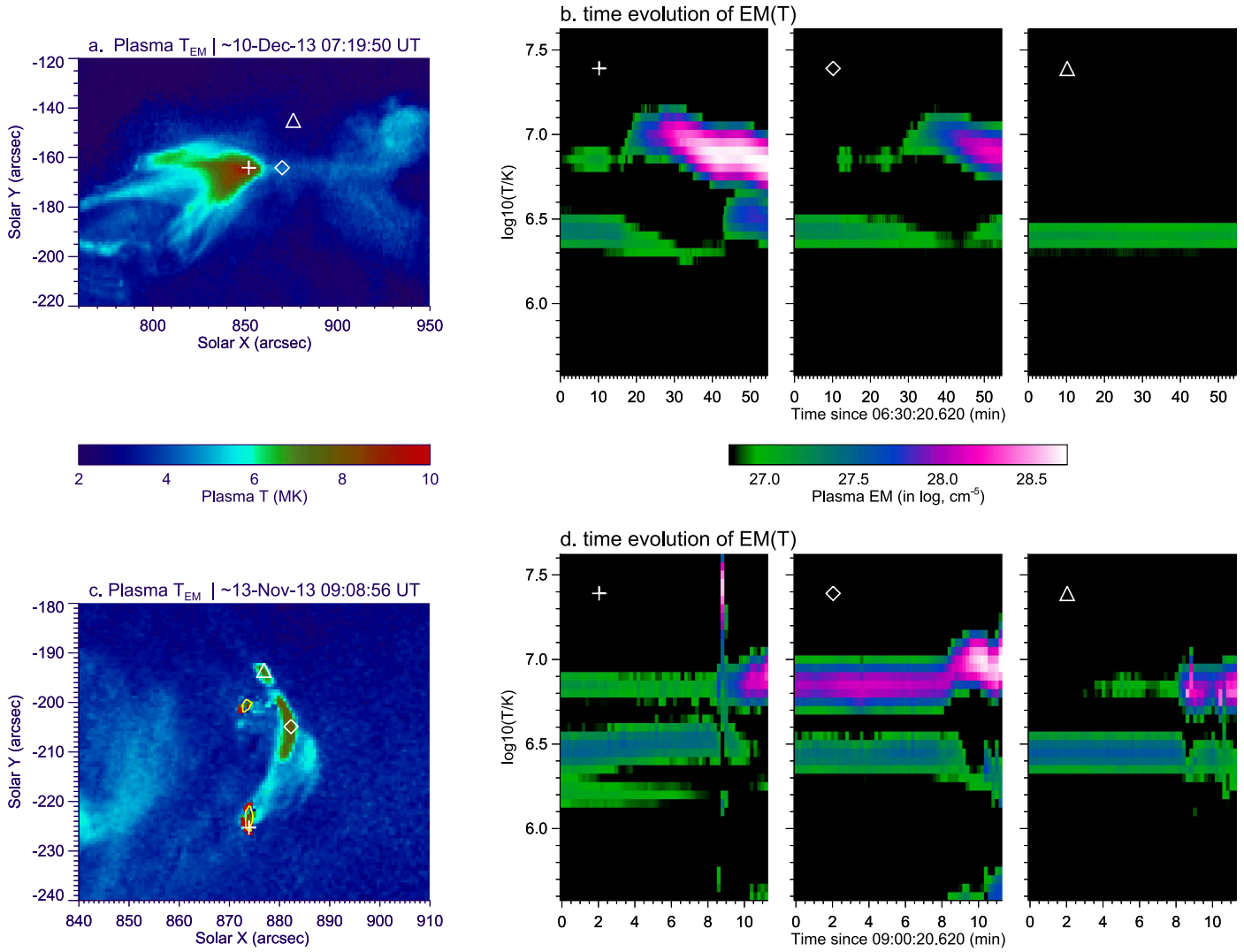

Figure 8. Time evolution of EM_T at different locations in the two flares. Panels (a) and (c): T_{EM} maps and selected locations. The yellow contours in (c) show the locations of the AIA pixels that have counts greater than 15,000 DN in the 193 Å channel, a level very close to the saturation of the AIA detectors. Panels (b) and (d): time evolutions of EM_T. These plots directly show the plasma heating and cooling at different flare sites.

of plasma EM in our examples clearly show different behavior of plasma heating at different locations of flares. They are useful for diagnostic of the heating mechanisms. (4) For plasma at temperatures beyond $\log_{10} T = 7.5$, all the codes returns lower temperatures than expected values. In such cases, more data are needed to further constrain the DEM.

Although improved, the code still fails to find solutions in some cases, and the results are not always in full agreement with X-ray data. We listed the possible causes and the limitations on the use of the code in the Appendix.

The DEM diagnostic provides valuable information by mapping the thermal plasma from ~0.3 MK to ~30 MK. With *SDO*'s continuous observations since 2010, the improved sparse inversion code allows the statistical study of plasma heating in a variety of situations, such as flare initiation, current sheets, cusps, super-arcade downflows, shocks, active regions, EIT waves, jets, etc.

RHESSI is a NASA Small Explorer Mission. The *GOES* is a joint effort of NASA and the National Oceanic and Atmospheric Administration (NOAA). AIA is an instrument on board *SDO*, a mission for NASA's Living with a Star program. *Hinode* is a Japanese mission developed and launched by ISAS/JAXA, with NAOJ as domestic partner and NASA and STFC (UK) as international partners. It is operated by these agencies in co-operation with ESA and NSC (Norway). Y.S., W.Q.G., and Y.P.L. acknowledge the Joint Research Fund in Astronomy (U1631242, U1731241) under the cooperative agreement between NSFC and CAS. This work is also supported by the Strategic Pioneer Program on Space Science, Chinese Academy of Sciences, grant Nos. XDA15052200, XDA15320300, and XDA15320301. Y.S. acknowledges the Thousand Young Talents Plan, a sub-program of the "1000 Talent Plan." A.M.V. acknowledges the Austrian Science Fund (FWF): P27292-N20. M.C.M.C. acknowledges support by NASA contract NNG04EA00C (*SDO*/AIA) and grant NNX14AI14G (Heliophysics Grand Challenges Research). I.G.H. is supported by a Royal Society University Fellowship.
Facilities: SDO(AIA), *RHESSI*, *Hinode*(XRT), *GOES*.

Appendix
Notes on the Use of the Code

We suggest setting the temperature bin size of 0.05 in $\log_{10} T$ (same as in the AIA TR), and to use re-binned AIA images with pixel size of 1.2 arcsec (same as the AIA spatial resolution).

There are many factors that could affect the DEM calculations.

1. Difficulties in cross-calibration between instruments.
2. AIA not being sensitive to plasma at flare temperatures, especially for $\log_{10} T$ above 7.5.
3. Inaccurate temperature response of the EUV instruments (due to changing detector performance).
4. Limited EUV channels, which means few data points to constrain the DEM. Different, equally probable solutions may co-exist.
5. Coronal abundances being used to derive the TR and thermal X-ray emission from EM results. For plasma heated at footpoints, the abundance may be different.
6. Estimation on uncertainties of intensities for each channel.
7. The time difference of a few seconds for images taken at different AIA channels possibly affecting the result in impulsive events.
8. Possible contribution from non-thermal EUV emissions that is not considered in the TR.
9. Pixels with very low intensity and pixels with intensities close to or exceeding the saturation level.
10. The DEM reconstruction methods themselves.
11. Structures with EUV emission that is not optically thin.

ORCID iDs

Yang Su https://orcid.org/0000-0002-4241-9921
Astrid M. Veronig https://orcid.org/0000-0003-2073-002X
Iain G. Hannah https://orcid.org/0000-0003-1193-8603
Mark C. M. Cheung https://orcid.org/0000-0003-2110-9753
Brian R. Dennis https://orcid.org/0000-0001-8585-2349
Gordon D. Holman https://orcid.org/0000-0002-2219-100X

References

Aschwanden, M. J., Boerner, P., Caspi, A., et al. 2015, SoPh, 290, 2733
Battaglia, M., & Kontar, E. P. 2013, ApJ, 779, 107
Caspi, A., & Lin, R. P. 2010, ApJL, 725, L161
Caspi, A., McTiernan, J. M., & Warren, H. P. 2014, ApJL, 788, L31
Cheung, M. C. M., Boerner, P., Schrijver, C. J., et al. 2015, ApJ, 807, 143
Christe, S., Shih, A. Y., Krucker, S., et al. 2016, in AGU Fall Meeting Abstracts, SH13A
Golub, L., Deluca, E., Austin, G., et al. 2007, SoPh, 243, 63
Golub, L., Deluca, E. E., Sette, A., & Weber, M. 2004, in ASP Conf. Ser. 325, The Solar-B Mission and the Forefront of Solar Physics, ed. T. Sakurai & T. Sekii (San Francisco, CA: ASP), 217
Hannah, I. G., & Kontar, E. P. 2012, A&A, 539, A146
Hudson, H. S., Strong, K. T., Dennis, B. R., et al. 1994, ApJL, 422, L25
Inglis, A. R., & Christe, S. 2014, ApJ, 789, 116
Khan, J. I., Hudson, H. S., & Mouradian, Z. 2004, A&A, 416, 323
Kosugi, T., Matsuzaki, K., Sakao, T., et al. 2007, SoPh, 243, 3
Lemen, J. R., Title, A. M., Akin, D. J., et al. 2012, SoPh, 275, 17
Lin, R. P., Dennis, B. R., Hurford, G. J., et al. 2002, SoPh, 210, 3
Lin, R. P., Schwartz, R. A., Pelling, R. M., & Hurley, K. C. 1981, ApJL, 251, L109
McTiernan, J. M., Kane, S. R., Loran, J. M., et al. 1993, ApJL, 416, L91
Milligan, R. O., & Dennis, B. R. 2009, ApJ, 699, 968
Motorina, G. G., & Kontar, E. P. 2015, Ge&Ae, 55, 995
Pesnell, W. D., Thompson, B. J., & Chamberlin, P. C. 2012, SoPh, 275, 3
Schmelz, J. T., Asgari-Targhi, M., Christian, G. M., Dhaliwal, R. S., & Pathak, S. 2015, ApJ, 806, 232
Shibata, K., & Magara, T. 2011, LRSP, 8, 6
Testa, P., Reale, F., Landi, E., DeLuca, E. E., & Kashyap, V. 2011, ApJ, 728, 30
Warren, H. P., Mariska, J. T., & Doschek, G. A. 2013, ApJ, 770, 116
Weber, M. A., Deluca, E. E., Golub, L., & Sette, A. L. 2004, in IAU Symp. 223, Multi-Wavelength Investigations of Solar Activity, ed. A. V. Stepanov, E. E. Benevolenskaya, & A. G. Kosovichev (Cambridge: Cambridge Univ. Press), 321
Woods, T. N., Caspi, A., Chamberlin, P. C., et al. 2017, ApJ, 835, 122
Wright, P. J., Hannah, I. G., Grefenstette, B. W., et al. 2017, ApJ, 844, 132
Zhu, C., Liu, R., Alexander, D., & McAteer, R. T. J. 2016, ApJL, 821, L29